Fluid–structure interaction modeling with nonmatching interface discretizations for compressible flow problems: simulating aircraft tail buffeting

Manoj R. Rajanna · **Monu Jaiswal** · **Emily L. Johnson** · **Ning Liu** ·
Artem Korobenko · **Yuri Bazilevs** · **Jim Lua** · **Nam Phan** · **Ming-Chen Hsu**

Abstract Many aerospace applications involve complex multiphysics in compressible flow regimes that are challenging to model and analyze. Fluid–structure interaction (FSI) simulations offer a promising approach to effectively examine these complex systems. In this work, a fully coupled FSI formulation for compressible flows is summarized. The formulation is developed based on an augmented Lagrangian approach and is capable of handling problems that involve nonmatching fluid–structure interface discretizations. The fluid is modeled with a stabilized finite element method for the Navier–Stokes equations of compressible flows and is coupled to the structure formulated using isogeometric Kirchhoff–Love shells. To solve the fully coupled system, a block-iterative approach is used. To demonstrate the framework's effectiveness for modeling industrial-scale applications, the FSI methodology is applied to the NASA Common Research Model (CRM) aircraft to study buffeting phenomena by performing an aircraft pitching simulation based on a prescribed time-dependent angle of attack.

M.R. Rajanna · N. Liu · J. Lua
Global Engineering & Materials, Inc., Princeton, NJ 08540, USA

M. Jaiswal · M.-C. Hsu (✉)
Department of Mechanical Engineering, Iowa State University,
Ames, IA 50011, USA
E-mail: jmchsu@iastate.edu

E.L. Johnson
Department of Aerospace and Mechanical Engineering,
University of Notre Dame, Notre Dame, IN 46556, USA

A. Korobenko
Department of Mechanical and Manufacturing Engineering,
University of Calgary, Calgary, AB T2N 1N4, Canada

Y. Bazilevs
School of Engineering, Brown University, Providence, RI 02912, USA

N. Phan
Structures Division, Naval Air Systems Command (NAVAIR),
Patuxent River, MD 20670, USA

1 Introduction

The aerospace industry has invested a considerable amount of time and resources into various research areas over the last few decades to advance the performance, efficiency, and safety of aircraft. Some notable efforts include enhancing external aerodynamic designs [1], improving the structural strength of aircraft materials [2], integrating lightweight structural components [3], and advancing the approaches for dynamic load prediction [4–6], fatigue damage evaluation [7, 8], and aeroelastic modeling and analysis [9–13]. The advancement of these primary research areas often relies on high-fidelity computational modeling, such as computational fluid dynamics (CFD), computational structural mechanics (CSM), and fluid–structure interaction (FSI) analysis. In aerospace applications, an FSI analysis is typically conducted through a loosely coupled scheme [14–16] to find the final equilibrium solution and configuration. This approach, however, tends to have convergence problems and may fail to accurately capture the nonlinear forces acting at the fluid–structure interface in complex situations, such as the aircraft buffeting problems [4–6] discussed in this paper.

Aircraft buffeting is a complex loading phenomenon characterized by random pressure oscillations on aircraft structures caused by unsteady airflow. Turbulent flow, normal shocks, and stalls can cause the flow to separate from the wing, which may lead to a buffeting response. This can occur in the wing itself or the empennage or tail region when unsteady flow excites a dynamic response from these surfaces. For aircraft operating under certain conditions, flow can also separate from external structures such as radomes, causing the turbulent wake to impinge on tail structures. Buffet load analysis is usually updated using regression

methods based on flight test data, such as peak-valley tables and Mach number-dynamic pressure usage data, but these methods heavily rely on real flight test data [5]. On the other hand, computational modeling of aircraft buffeting is challenging due to aerodynamic nonlinearities and complex structural components of the aircraft.

To model and predict aircraft tail buffeting phenomena, this work adopts a validated fully coupled nonmatching interface-based compressible flow FSI methodology developed by Rajanna et al. [17] based on the augmented Lagrangian approach [18]. The FSI framework makes use of the stabilized finite element-based Navier–Stokes equation of compressible flow [19, 20] to model the fluid, and the isogeometric analysis (IGA) based rotation-free Kirchhoff–Love thin-shell structural formulation [21–23] to model the structure. The combined use of finite elements for fluids and IGA for structures has proven to provide an effective balance between accuracy, robustness, and speed for FSI simulations [24–27].

The present work uses this FSI formulation to simulate the unsteady flow around the NASA Common Research Model (CRM) aircraft [28–30]. A time-dependent simulation for varying angles of attack (AOAs) is performed to study and understand the initiation and effects of buffeting as a function of the angle of attack. Different flow and structural quantities of interest have been analyzed at different time instances during the FSI simulation. The fluid flow around the aircraft is modeled using linear finite elements, and only the aircraft's horizontal stabilizer is modeled using cubic non-uniform rational B-splines (NURBS) to study its structural response. The aircraft aerodynamic modeling has been validated using 3D flow simulations over the NASA CRM wing-body configuration at transonic conditions in Rajanna et al. [20].

This paper is outlined as follows. Section 2 presents the FSI framework for compressible flows, summarizes the fluid and structural formulations, and concludes with a discussion of time integration and FSI coupling techniques. In Section 3, the compressible flow FSI framework is applied to simulate flow around the CRM aircraft and predict the structural response of its horizontal tail due to the induced buffeting phenomena. Conclusions are drawn in Section 4.

2 FSI formulation for compressible flows

The fully coupled FSI formulation for compressible flow problems with nonmatching fluid–structure interface discretizations is presented here. In what follows, superscripts "f" and "s" denote quantities associated with the fluid and structural subproblems, respectively. Ω_t^{f} and $\Omega_t^{\mathrm{s}} \in \mathbb{R}^d$, $d \in \{2, 3\}$ denote the spatial domains of the fluid and structural mechanics problems, respectively, at time t, with Γ_t^{f} and Γ_t^{s} representing their boundaries. $\Gamma_t^{\mathrm{I}} \in \mathbb{R}^d$ repre-

sent the interface between the fluid and structural domains. $\mathbf{Y}^{\mathrm{f}} = [p \ \mathbf{u}^{\mathrm{f}} \ T^{\mathrm{f}}]^{\mathrm{T}}$ is the vector of pressure-primitive variables, where $p, \mathbf{u}^{\mathrm{f}}$, and T^{f} are the pressure, velocity and temperature of the fluid, respectively. $\mathbf{y}^{\mathrm{s}}$ denotes the structural displacement, with $\mathbf{u}^{\mathrm{s}}$ being its velocity defined as the material time derivative of $\mathbf{y}^{\mathrm{s}}$. Let $\mathcal{S}^{\mathrm{f}}$ and $\mathcal{S}^{\mathrm{s}}$ be the trial function spaces for the fluid and structural mechanics variables, respectively, with $\mathcal{V}^{\mathrm{f}}$ and $\mathcal{V}^{\mathrm{s}}$ being the corresponding test function spaces. Let the superscript h denote the corresponding variable in the discrete space. The semi-discrete variational problem for the compressible flow FSI system is given by: Find $\mathbf{Y}^{\mathrm{f},h} = [p^h \ \mathbf{u}^{\mathrm{f},h} \ T^{\mathrm{f},h}]^{\mathrm{T}} \in \mathcal{S}^{\mathrm{f},h}$ and $\mathbf{y}^{\mathrm{s},h} \in \mathcal{S}^{\mathrm{s},h}$ such that for all test functions $\mathbf{W}^{\mathrm{f},h} = [q^h \ \mathbf{w}^{\mathrm{f},h} \ w_T^{\mathrm{f},h}]^{\mathrm{T}} \in \mathcal{V}^{\mathrm{f},h}$ and $\mathbf{w}^{\mathrm{s},h} \in \mathcal{V}^{\mathrm{s},h}$,

$$B_{\mathrm{STAB}}^{\mathrm{f}}\left(\mathbf{W}^{\mathrm{f},h}, \mathbf{Y}^{\mathrm{f},h}\right) + B_{\mathrm{WBC}}^{\mathrm{f}}\left(\mathbf{W}^{\mathrm{f},h}, \mathbf{Y}^{\mathrm{f},h}\right) - F^{\mathrm{f}}\left(\mathbf{W}^{\mathrm{f},h}\right)$$
$$+ B_{\mathrm{KL}}^{\mathrm{s}}\left(\mathbf{w}^{\mathrm{s},h}, \mathbf{y}^{\mathrm{s},h}\right) - F_{\mathrm{KL}}^{\mathrm{s}}\left(\mathbf{w}^{\mathrm{s},h}\right) = 0 \,, \tag{1}$$

where B^{f}, B^{s}, F^{f}, and F^{s} are the semi-linear forms and linear functionals corresponding to the fluid and structural mechanics problems, respectively. Their detailed expressions are given below.

For the fluid mechanics part of the FSI problem, let Ω_t^{f} be divided into N_{el} spatial finite elements, each denoted by Ω_e^{f}, and let Γ_t^{f} be decomposed into N_{eb} surface elements, where the bth element is denoted by Γ_b^{f}. Let the mesh defined by $\bigcup_e \overline{\Omega_e^{\mathrm{f}}}$ deform with a velocity field $\hat{\mathbf{u}}$, and let the boundary Γ_t^{I} move with velocity $\mathbf{u}^{\mathrm{s}}$. Note that Ω_e^{f} and Γ_b^{f} remain time dependent, but the subscript t is omitted for notational convenience.

$B_{\mathrm{STAB}}^{\mathrm{f}}$ in Eq. (1) is the stabilized discretizations of B^{f} using both streamline upwind/Petrov–Galerkin (SUPG) [31–44] and discontinuity-capturing (DC) [45–56] operators and is given by

$$B_{\mathrm{STAB}}^{\mathrm{f}}\left(\mathbf{W}^{\mathrm{f}}, \mathbf{Y}^{\mathrm{f}}\right) =$$
$$\int_{\Omega_t^{\mathrm{f}}} \mathbf{W}^{\mathrm{f}} \cdot \left(\mathbf{A}_0 \mathbf{Y}_{,t}^{\mathrm{f}} + \left(\mathbf{A}_i^{\mathrm{adv}\backslash\mathrm{p}} + \mathbf{A}_i^{\mathrm{sp}} - \hat{u}_i \mathbf{A}_0\right) \mathbf{Y}_{,i}^{\mathrm{f}}\right) \mathrm{d}\Omega$$
$$- \int_{\Omega_t^{\mathrm{f}}} \mathbf{W}_{,i}^{\mathrm{f}} \cdot \left(\mathbf{A}_i^p \mathbf{Y}^{\mathrm{f}} - \mathbf{K}_{ij} \mathbf{Y}_{,j}^{\mathrm{f}}\right) \mathrm{d}\Omega$$
$$+ \sum_{e=1}^{N_{\mathrm{el}}} \int_{\Omega_e^{\mathrm{f}}} \left(\left(\mathbf{A}_i^{\mathrm{ALE}}\right)^{\mathrm{T}} \mathbf{W}_{,i}^{\mathrm{f}}\right) \cdot \left(\mathbf{A}_0^{-1} \hat{\boldsymbol{\tau}}_{\mathrm{SUPG}}\right) \mathbf{Res}(\mathbf{Y}) \, \mathrm{d}\Omega$$
$$+ \sum_{e=1}^{N_{\mathrm{el}}} \int_{\Omega_e^{\mathrm{f}}} \mathbf{W}_{,i}^{\mathrm{f}} \cdot \left(\hat{\kappa}_{\mathrm{DC}} \mathbf{A}_0\right) \mathbf{Y}_{,i}^{\mathrm{f}} \, \mathrm{d}\Omega \,, \tag{2}$$

where $i = 1, \ldots, d$ for a spatial domain of dimension d, $\hat{u}_i$ is the ith component of the domain velocity $\hat{\mathbf{u}}$, $\mathbf{A}$'s and $\mathbf{K}_{ij}$ are the arbitrary Lagrangian–Eulerian (ALE) version of the Euler Jacobian and diffusivity matrices, respectively, for the Navier–Stokes equations of compressible flows [17], $(\cdot)_{,i}$ denotes a spatial gradient, and $(\cdot)_{,t}$ denotes a partial time derivative taken with respect to a fixed spatial coordinate

in the referential domain. The convention used for i applies to j, k, and l, and the Einstein summation convention on repeated indices is used throughout. In Eq. (2), **Res** is the fluid residual, $\hat{\boldsymbol{\tau}}_{\text{SUPG}}$ is the SUPG stabilization matrix, and $\hat{\kappa}_{\text{DC}}$ is the DC parameter. Their details can be found in Rajanna et al. [17].

The weak boundary condition operator $B_{\text{WBC}}^{\text{f}}$ in Eq. (1) is defined at the fluid–structure interface as

$$
\begin{aligned}
B_{\text{WBC}}^{\text{f}} & \left(\mathbf{W}^{\text{f}}, \mathbf{Y}^{\text{f}} \right) = \\
& - \sum_{b=1}^{N_{\text{eb}}} \int_{\Gamma_b^{\text{I}}} \mathbf{w}^{\text{f}} \cdot \left(\boldsymbol{\sigma}^{\text{f}}(\mathbf{u}^{\text{f}}, p) \mathbf{n}^{\text{f}} \right) d\Gamma \\
& - \sum_{b=1}^{N_{\text{eb}}} \int_{\Gamma_b^{\text{I}}} \left(\delta \boldsymbol{\sigma}^{\text{f}}(\mathbf{w}^{\text{f}}, q) \mathbf{n}^{\text{f}} \right) \cdot \left(\mathbf{u}^{\text{f}} - \Pi^{\text{f}} \mathbf{u}^{\text{s}} \right) d\Gamma \\
& - \sum_{b=1}^{N_{\text{eb}}} \int_{(\Gamma_b^{\text{I}})^-} \mathbf{w}^{\text{f}} \cdot \rho^{\text{f}} \left(\left(\mathbf{u}^{\text{f}} - \hat{\mathbf{u}} \right) \cdot \mathbf{n}^{\text{f}} \right) \left(\mathbf{u}^{\text{f}} - \Pi^{\text{f}} \mathbf{u}^{\text{s}} \right) d\Gamma \\
& + \sum_{b=1}^{N_{\text{eb}}} \int_{\Gamma_b^{\text{I}}} \mathbf{w}^{\text{f}} \cdot \tau_\mu^{\text{B}} \left(\mathbf{u}^{\text{f}} - \Pi^{\text{f}} \mathbf{u}^{\text{s}} \right) d\Gamma \\
& + \sum_{b=1}^{N_{\text{eb}}} \int_{\Gamma_b^{\text{I}}} \left(\mathbf{w}^{\text{f}} \cdot \mathbf{n}^{\text{f}} \right) \tau_\lambda^{\text{B}} \left(\left(\mathbf{u}^{\text{f}} - \Pi^{\text{f}} \mathbf{u}^{\text{s}} \right) \cdot \mathbf{n}^{\text{f}} \right) d\Gamma \\
& - \sum_{b=1}^{N_{\text{eb}}} \int_{\Gamma_b^{\text{I}}} w_T^{\text{f}} \kappa^{\text{f}} \nabla T^{\text{f}} \cdot \mathbf{n}^{\text{f}} d\Gamma \\
& - \sum_{b=1}^{N_{\text{eb}}} \int_{\Gamma_b^{\text{I}}} \kappa^{\text{f}} \nabla w_T^{\text{f}} \cdot \mathbf{n}^{\text{f}} \left(T^{\text{f}} - T^{\text{B}} \right) d\Gamma \\
& - \sum_{b=1}^{N_{\text{eb}}} \int_{(\Gamma_b^{\text{I}})^-} w_T^{\text{f}} \rho^{\text{f}} c_{\text{v}} \left(\left(\mathbf{u}^{\text{f}} - \hat{\mathbf{u}} \right) \cdot \mathbf{n}^{\text{f}} \right) \left(T^{\text{f}} - T^{\text{B}} \right) d\Gamma \\
& + \sum_{b=1}^{N_{\text{eb}}} \int_{\Gamma_b^{\text{I}}} w_T^{\text{f}} \tau_\kappa^{\text{B}} \left(T^{\text{f}} - T^{\text{B}} \right) d\Gamma ,
\end{aligned}
\tag{3}
$$

where $\boldsymbol{\sigma}^{\text{f}}$ is the fluid Cauchy stress and $\delta\boldsymbol{\sigma}^{\text{f}}$ is its corresponding variation, $\mathbf{n}^{\text{f}}$ is the unit outward normal vector to the fluid domain, ρ^{f} is the fluid density, T^{B} is the prescribed temperature on the structure boundary, and κ^{f} is the thermal conductivities of the fluid. A calorically perfect gas is assumed in this work, and the fluid thermal conductivity is calculated by $\kappa^{\text{f}} = \mu c_p / Pr$, where μ is the fluid dynamic viscosity, $c_p = \gamma c_{\text{v}}$ is the specific heat at constant pressure, $c_{\text{v}} = R/(\gamma - 1)$ is the specific heat at constant volume, γ is the heat capacity ratio, R is the ideal gas constant, and Pr is the Prandtl number.

In Eq. (3), $\Gamma_b^{\text{I}} = \Gamma_b^{\text{f}} \bigcap \Gamma_t^{\text{I}}$, $(\cdot)^-$ denotes the "inflow" part of Γ^{I}, where $(\mathbf{u}^{\text{f}} - \hat{\mathbf{u}}) \cdot \mathbf{n}^{\text{f}} < 0$, Π^{f} is a projection operator onto the space spanned by the fluid basis functions restricted to the fluid–structure interface, the mesh velocity $\hat{\mathbf{u}}$ is obtained using $\hat{\mathbf{u}} = \Pi^{\text{f}} \mathbf{u}^{\text{s}}$, and $\tau_\mu^{\text{B}} = C_I^{\text{B}} \mu / h_n$, $\tau_\lambda^{\text{B}} = C_I^{\text{B}} |\lambda| / h_n$, and $\tau_\kappa^{\text{B}} = C_I^{\text{B}} \kappa / h_n$ are stabilization parameters for the symmetric

Nitsche's method, where C^{B} is a positive constant obtained from an inverse estimate, $\lambda = -2\mu/3$ is the second coefficient of viscosity, and h_n is the element size in the direction normal to the wall.

F^{f} in Eq. (1) is given by

$$
F^{\text{f}} \left(\mathbf{W}^{\text{f}} \right) = \int_{\Omega_t^{\text{f}}} \mathbf{W}^{\text{f}} \cdot \mathbf{S}^{\text{f}} \, d\Omega + \int_{\Gamma_t^{\text{f,H}}} \mathbf{W}^{\text{f}} \cdot \mathbf{H}^{\text{f}} \, d\Gamma ,
\tag{4}
$$

where $\mathbf{S}^{\text{f}}$ is the fluid source term, and $\Gamma_t^{\text{f,H}}$ denotes the portion of Γ_t^{f} where the fluid traction and heat flux boundary conditions $\mathbf{H}^{\text{f}}$ are enforced.

For the structural mechanics part of the FSI problem, this work incorporates an isogeometric Kirchhoff–Love thin-shell formulation [21–23]. B_{KL}^{s} and F_{KL}^{s} in Eq. (1) are given by

$$
\begin{aligned}
B_{\text{KL}}^{\text{s}} \left(\mathbf{w}^{\text{s}}, \mathbf{y}^{\text{s}} \right) = & \int_{\mathcal{S}_0^{\text{s}}} \mathbf{w}^{\text{s}} \cdot \rho^{\text{s}} h_{\text{th}} \left. \frac{\partial^2 \mathbf{y}^{\text{s}}}{\partial t^2} \right|_{\mathbf{X}} d\mathcal{S} \\
& + \int_{\mathcal{S}_0^{\text{s}}} \int_{-\frac{h_{\text{th}}}{2}}^{\frac{h_{\text{th}}}{2}} \delta \mathbf{E} : \mathbf{S} \, d\xi^3 \, d\mathcal{S}
\end{aligned}
\tag{5}
$$

and

$$
\begin{aligned}
F_{\text{KL}}^{\text{s}} \left(\mathbf{w}^{\text{s}} \right) = & \int_{\mathcal{S}_0^{\text{s}}} \mathbf{w}^{\text{s}} \cdot \rho^{\text{s}} h_{\text{th}} \mathbf{f}^{\text{s}} \, d\mathcal{S} + \int_{\mathcal{S}_0^{\text{s,h}}} \mathbf{w}^{\text{s}} \cdot \mathbf{h}^{\text{s}} \, d\mathcal{S} \\
& + \int_{\Gamma_t^{\text{I}}} \mathbf{w}^{\text{s}} \cdot \left(\Pi^{\text{s}} \mathbf{t}^{\text{f}} \right) d\Gamma ,
\end{aligned}
\tag{6}
$$

where $\mathcal{S}_0^{\text{s}}$ is the shell midsurface in the reference configuration, Γ_t^{I} is the shell midsurface in the deformed configuration, h_{th} is the shell thickness, ρ^{s} is the density of the structure, $\left. \frac{\partial(\cdot)}{\partial t} \right|_{\mathbf{X}}$ is the time derivative holding the material coordinates $\mathbf{X}$ fixed, $\mathbf{E}$ is the Green–Lagrange strain tensor, $\delta\mathbf{E}$ is the variation of $\mathbf{E}$ corresponding to displacement variation $\mathbf{w}^{\text{s}}$, $\mathbf{S}$ is the second Piola–Kirchhoff stress tensor, $\xi^3 \in [-h_{\text{th}}/2, h_{\text{th}}/2]$ is the through-thickness coordinate, $\mathbf{f}^{\text{s}}$ is the body force, $\mathcal{S}_0^{\text{s,h}}$ denotes the portion of $\mathcal{S}_0^{\text{s}}$ where only the traction boundary condition $\mathbf{h}^{\text{s}}$ is enforced, Π^{s} is a projection operator onto the space spanned by the structural basis functions restricted to the fluid–structure interface, and $\mathbf{t}^{\text{f}}$ is the discrete counterpart of the fluid traction vector defined as

$$
\mathbf{t}^{\text{f}} = -\boldsymbol{\sigma}^{\text{f}} \mathbf{n}^{\text{f}} - \tau_\mu^{\text{B}} \left(\Pi^{\text{f}} \mathbf{u}^{\text{s}} - \mathbf{u}^{\text{f}} \right) - \left(\tau_\lambda^{\text{B}} \left(\Pi^{\text{f}} \mathbf{u}^{\text{s}} - \mathbf{u}^{\text{f}} \right) \cdot \mathbf{n}^{\text{f}} \right) \mathbf{n}^{\text{f}} .
\tag{7}
$$

Throughout this work, the St. Venant–Kirchhoff material model is used; the stress–strain relationship is expressed as $\mathbf{S} = \mathbb{C} \mathbf{E}$, where $\mathbb{C}$ is the constitutive material tensor.

In this work, both Π^{f} and Π^{s} are defined to be L^2-projection operators, which globally conserve forces and moments acting on the fluid and structure [18]. For the time integration of the FSI equations and coupling strategies, this work applies the generalized-α method [57–59] to integrate the semi-discrete ALE formulation for compressible
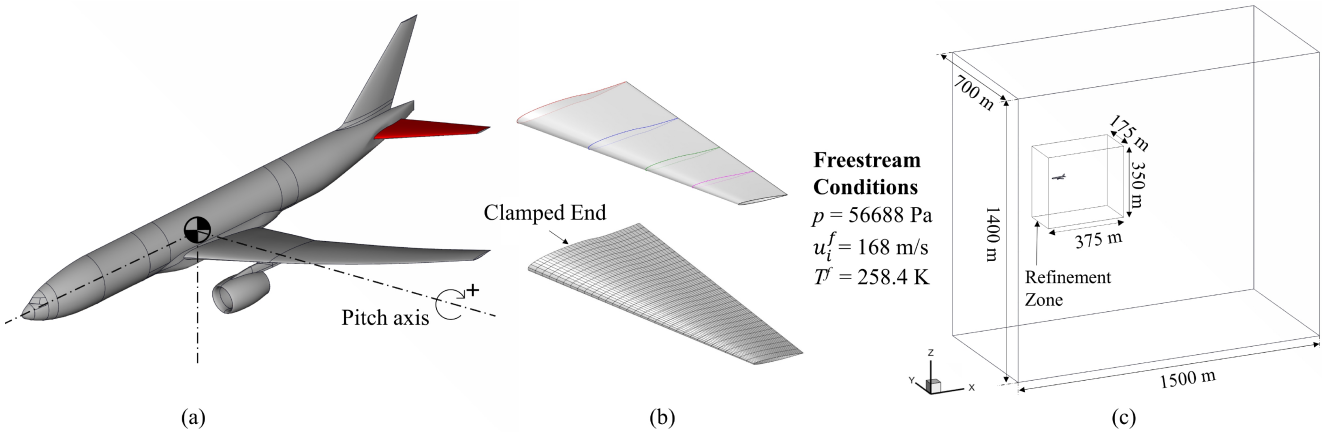
Fig. 1: (a) Left half of the wing-body-tail CRM CAD geometry model used to simulate the tail buffeting problem. (b) CAD geometry and computational structural mechanics mesh of the horizontal tail based on NURBS. The connection between the horizontal tail root and the fuselage is simulated using a clamped boundary condition. (c) Computational domain and boundary conditions to simulate aircraft pitching. Freestream conditions are applied to all outer boundary surfaces of the fluid domain.
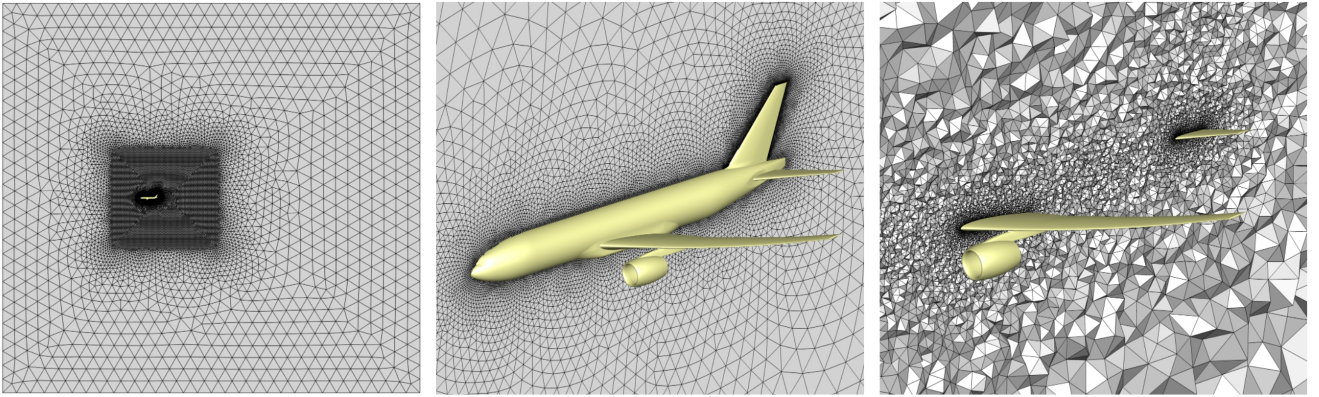

Fig. 2: Computational fluid mechanics mesh for the aircraft buffeting simulation.

flow problems and the Lagrangian formulation for structural mechanics applications. The combined fluid, structure, and mesh motion discrete residuals are converged to zero at each time step using a block-iterative FSI coupling approach [18, 60–62], which is highly efficient for problems with nonmatching fluid and structural discretizations. Newton–Raphson iterations are repeated until convergence to an appropriately coupled discrete solution is achieved.

3 Application to simulating aircraft buffeting

The compressible flow FSI formulation for nonmatching interface discretizations presented in Section 2 was thoroughly validated in Rajanna et al. [17]. To demonstrate its high-fidelity modeling capability for a full-scale aircraft subject to an aggressive operational condition, we select the Common Research Model (CRM) [30] to study the occurrence of buffeting events when performing maneuvers. In this section, we use the proposed FSI framework to simulate a time-dependent varying angle of attack simulation of the CRM

aircraft and study the effects of buffeting phenomena by observing different flow and structural quantities of interest. The aerodynamic modeling of the aircraft was validated in Rajanna et al. [20] using flow simulations of a CRM wing-body configuration at transonic conditions.

3.1 Problem setup

To model the aircraft buffeting problem, we assume the aircraft is flying under cruise conditions at a specified speed and performs a consecutive pitch-up and pitch-down maneuver. The aircraft is assumed to be rigid everywhere except for the horizontal tail, which is flexible and cantilevered (clamped) to the fuselage. The pitching maneuver is executed in two stages. First, the aircraft is positioned at a zero-degree angle of attack, and uniform freestream (far-field) conditions are prescribed on all outer boundaries of the fluid mechanics domain to simulate cruising conditions. Once the flow is fully developed, the pitching motion is
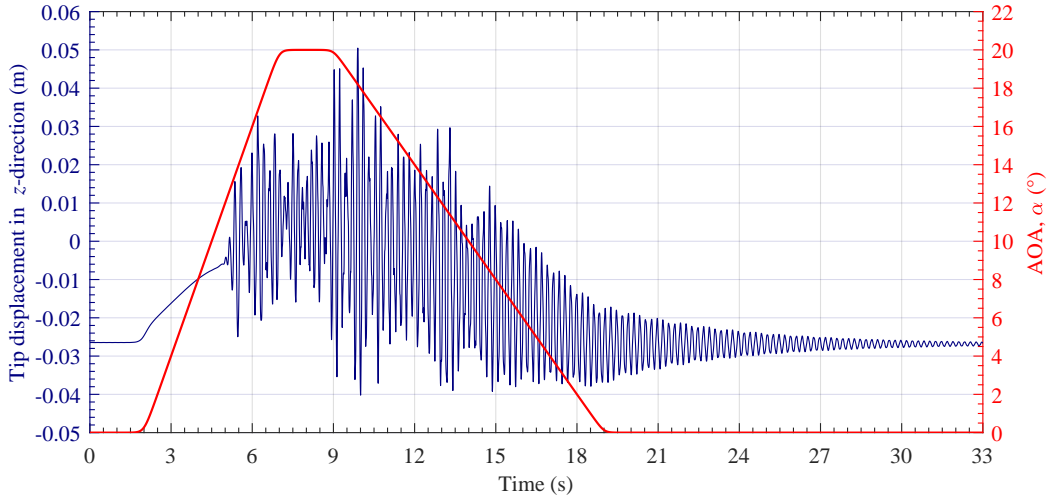
Fig. 3: Time history of the prescribed input Angle of Attack (AOA) and horizontal tail tip displacement in the z-direction.
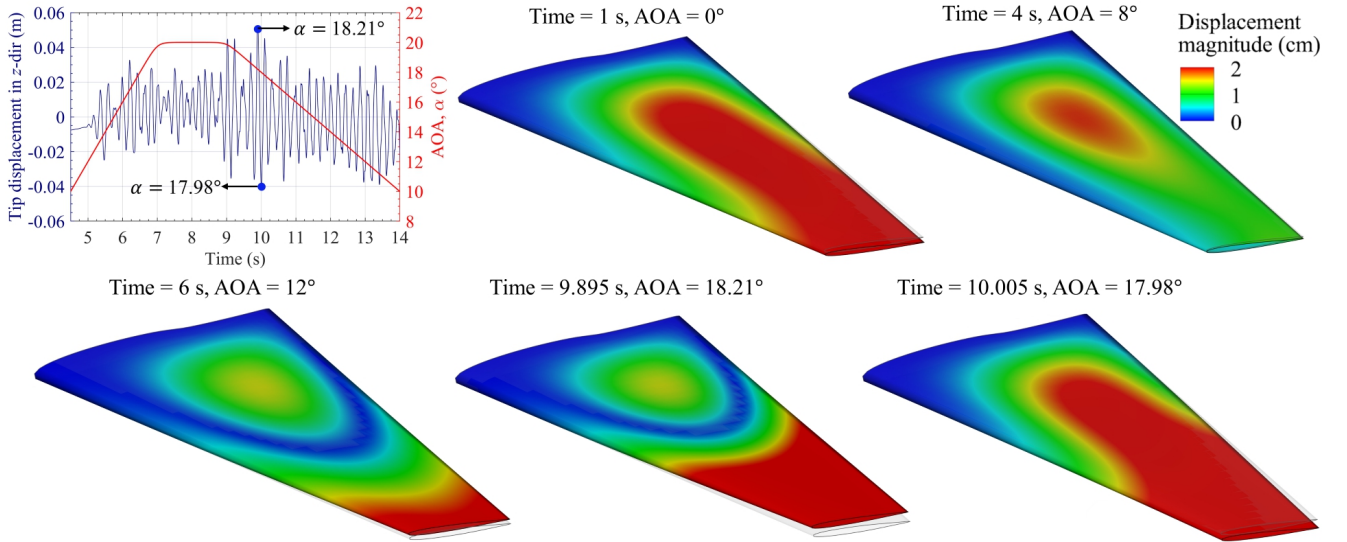

Fig. 4: Displacement magnitude contour of the horizontal tail overlapped with its reference configuration (colored in gray). The deformation is scaled up 5 times for visualization. The view angle is rotated to align with the pitch angle.

prescribed for the entire computational domain while keeping the freestream conditions fixed. The far-field air velocity, pressure, and temperature are set to $u_1^f = 168$ m/s, $p = 56.688$ kPa, and $T^f = 258.4$ K, respectively, which result in a Mach number of 0.52. The no-slip velocity and stagnation temperature of $T^B = 272.4$ K are imposed on the aircraft surface as weak boundary conditions. The stagnation temperature is calculated by $T^B = (1 + 0.5(\gamma - 1)M_\infty^2)T_\infty$, where M_∞ and T_∞ are the far-field Mach number and temperature, respectively. Standard air properties of $Pr = 0.72$, $\gamma = 1.4$, and $R = 288.293$ J/(kg·K) are used. The viscosity of the air is assumed to be constant and is set to $\mu = 1.758 \times 10^{-5}$ kg/(m·s). The pitching motion is prescribed by rotating the entire fluid domain about the quarter-chord pitch axis of the mean aerodynamic chord of the aircraft at a rate of 4°/s and −2°/s while pitching up and down,

respectively. During the maneuver, the aircraft is subjected to a maximum angle of attack of 20°.

Figure 1 illustrates the geometry model of an idealized aircraft, horizontal stabilizer tail, and the computational domain used to perform this study. The aircraft model has a fuselage length of 62.74 m, a wing semispan of 29.38 m, and a tail semispan of 10.67 m. In this study, the FSI simulation is performed by assuming only the left horizontal tail of the aircraft as the structural part of the FSI problem. The tail deformation is governed by the isogeometric Kirchhoff–Love shell formulation with a St. Venant–Kirchhoff material model. Figure 1(b) shows the geometry of the horizontal tail, defined as the combination of a stabilizer and an elevator in this work. The tail structure is idealized (without internal spars and ribs) and has a root chord length of 5.3 m
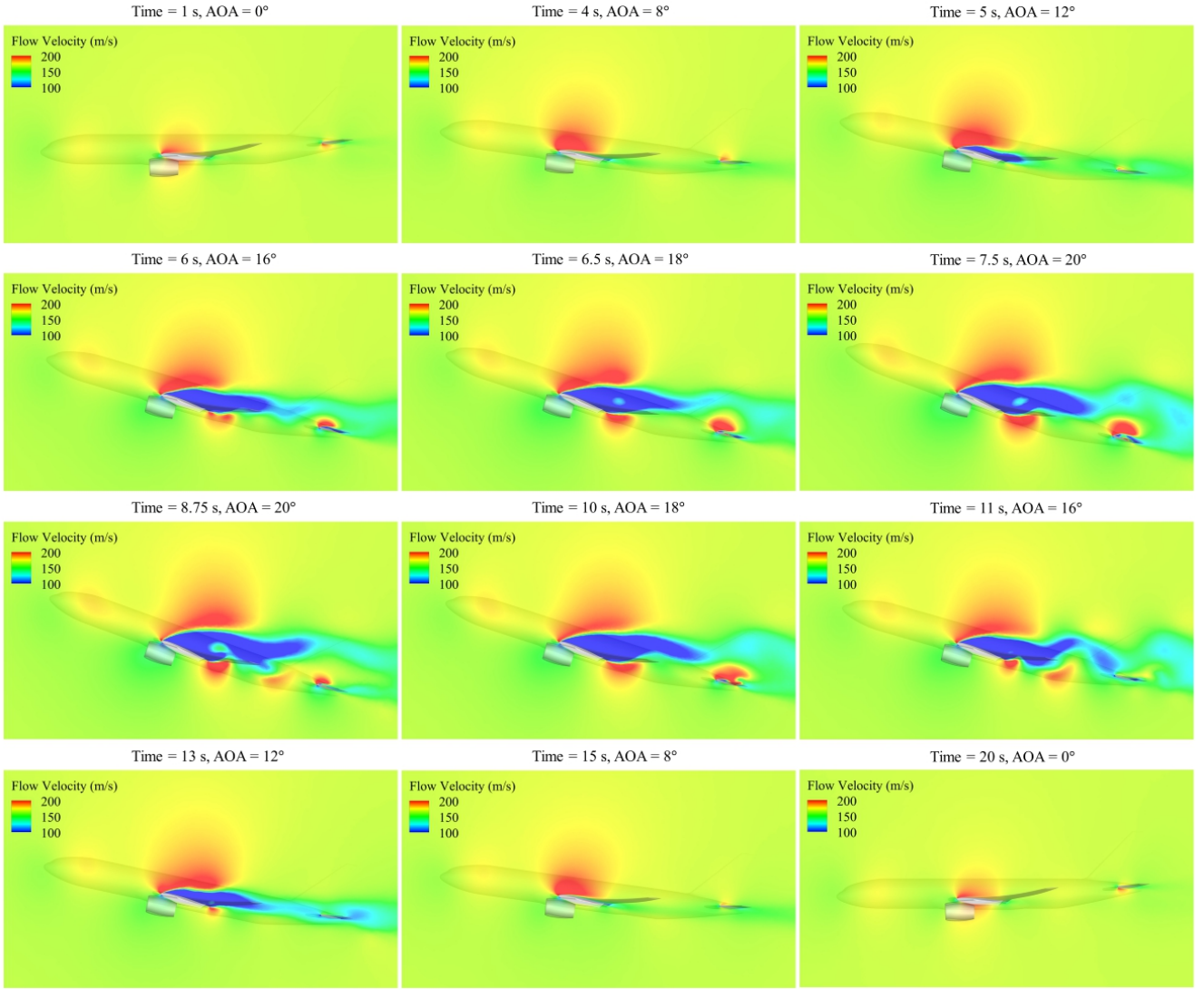
Fig. 5: Fluid flow velocity contour along the midspan of the horizontal tail at different time instances.

and tip chord length of 2.23 m. The NURBS surface mesh of the stabilizer is comprised of 2144 cubic elements and 2450 control points. The material is assumed to be linearly elastic with Young's modulus of $E = 70$ GPa, a Poisson's ratio of $\nu = 0.35$, a density of $\rho^s = 2700$ kg/m^3, and a thickness of $h_{th} = 8$ cm. Figure 2 shows the computational volume mesh generated using tetrahedral elements. The computational mesh is comprised of 6,486,616 linear tetrahedral elements. An element size of 0.1 m is used to discretize the wing and tail surfaces of the fluid domain, and an element size of 0.2 m is used for the remaining aircraft surfaces. The maximum element size in the mesh refinement zone is 5 m with an element growth ratio of 1.15. A time step size of $\Delta t = 0.5 \times 10^{-3}$ s is used in this simulation.

During the aircraft pitching simulation, the motion of the horizontal tail and the fluid domain are dominated by the rotational motion due to pitching. This type of large rotational motion can be common in maneuvering simulations when rotating about yaw, roll, and pitch axes. For structures, solving for large rotations can become harder to converge, especially for long-term integration. In the case of the fluid domain, the linear elastostatics problem [63–65] is solved to determine the interior mesh motion, which may lead to undesired mesh distortion for large rotations. To circumvent this difficulty, following the procedure in Bazilevs et al. [66], the displacements of the structure and the fluid domain interior can be decomposed into their respective rotation and deflection components. The rotational motion is handled exactly based on the prescribed pitch angle for both the fluid domain and the structure, and the deflection part is solved using the Kirchhoff–Love shell for the structure and linear elastostatics for the fluid domain interior. We combine the exact rotations and time-discrete deflections to get a total discrete solution at each time step.
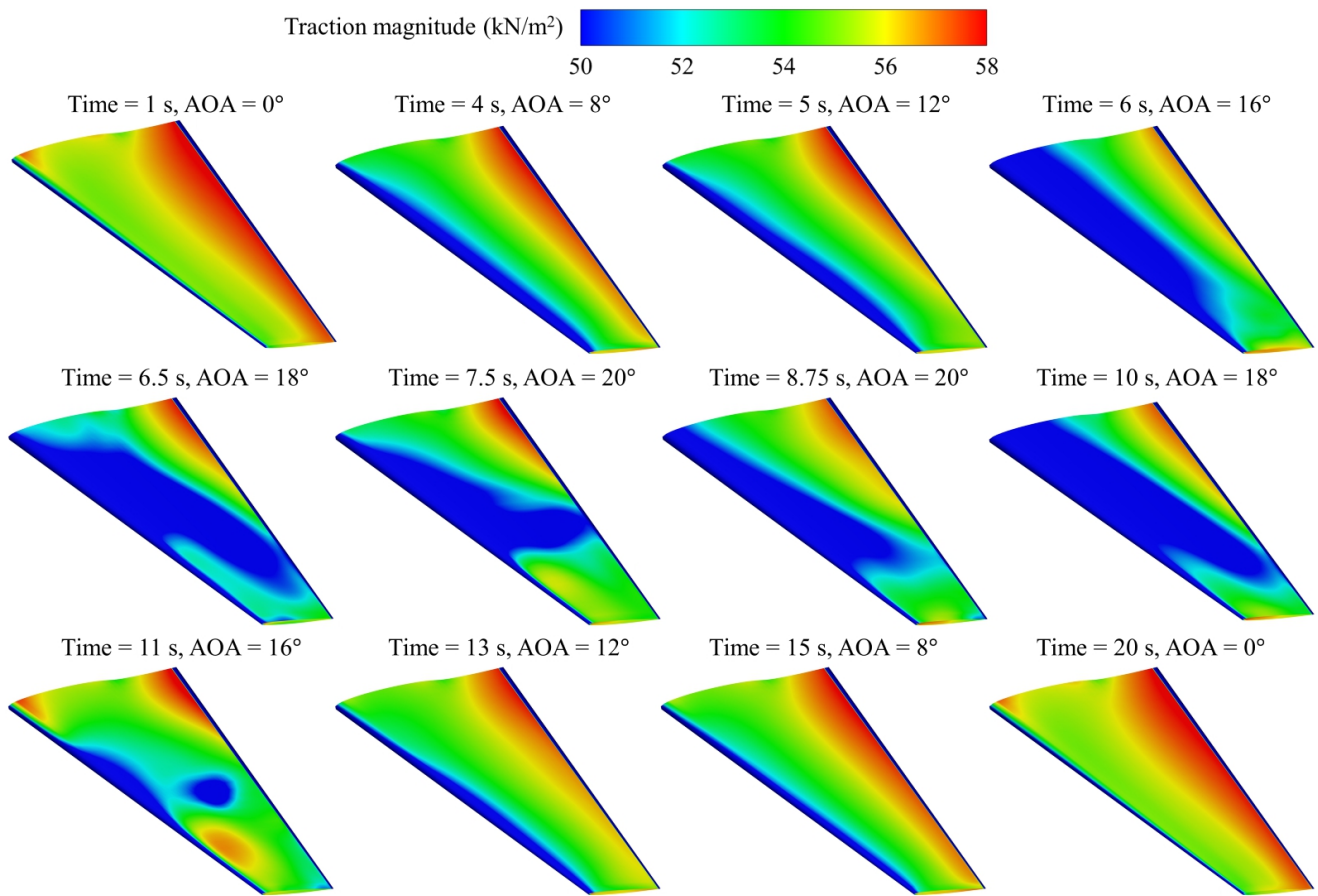
Fig. 6: Contour plot of the fluid traction magnitude acting on the horizontal tail at different time instances. The view angle is rotated to align with the pitch angle.

3.2 Computational results

Figure 3 shows the prescribed input angle of attack to perform the pitch maneuver and the time history of the tip displacement of the left horizontal tail obtained using the proposed FSI formulation. The tip displacement results demonstrate severe tail vibration at higher aircraft angles of attack. The amplitude of the tip oscillation is almost negligible during the pitching up motion between 0° and 12° angle of attack, but it experiences a sudden and nonlinear rise in magnitude beyond the 12° angle. The significant displacement can be attributed to the turbulent wake produced by the wing that directly impacts the tail. This wake is particularly intense at higher angles of attack and can further increase the vibration of the tail. The vibration is exacerbated when a second wave of turbulent wake flow from the wing strikes the tail at an angle of 18° during downward pitching, resulting in the highest recorded displacement of the tip. Figure 4 illustrates the deformation of the horizontal tail in comparison with the reference configuration at different time points, including the instances where the highest and lowest displacements are observed at angles of attack of 18.21° and 17.98°,

respectively. To visually demonstrate the flow behavior, Figure 5 displays the fluid velocity distribution along the midspan of the horizontal tail, and Figure 6 presents the fluid traction magnitude exerted on the tail structure at different time instances and angles of attack. These findings exhibit the consistent airflow around the wing and tail regions when the angle of attack is below 12°. However, when the angle of attack surpasses 12°, significant airflow detachment from the wing and related flow disruptions in the aircraft's tail region become apparent. The same phenomena can also be observed in Figure 6, which shows the irregular variation of traction magnitude on the tail beyond 12° angle. After 15 seconds into the pitch-down maneuver, the flow over the wings becomes fully attached at an angle of attack of 8°, as depicted in Figure 5; however, the vibration in the tail still exists, as illustrated in Figure 3. The vibration in the tail after the flow re-attaches can be primarily categorized as damped vibration, as the clamped horizontal tail acts as an under-damped system. The oscillation dissipates on its own as the aerodynamic damping acts steadily on the tail after the aircraft returns to its original position at the zero-degree angle of attack. The behavior of the horizontal tail from 12°
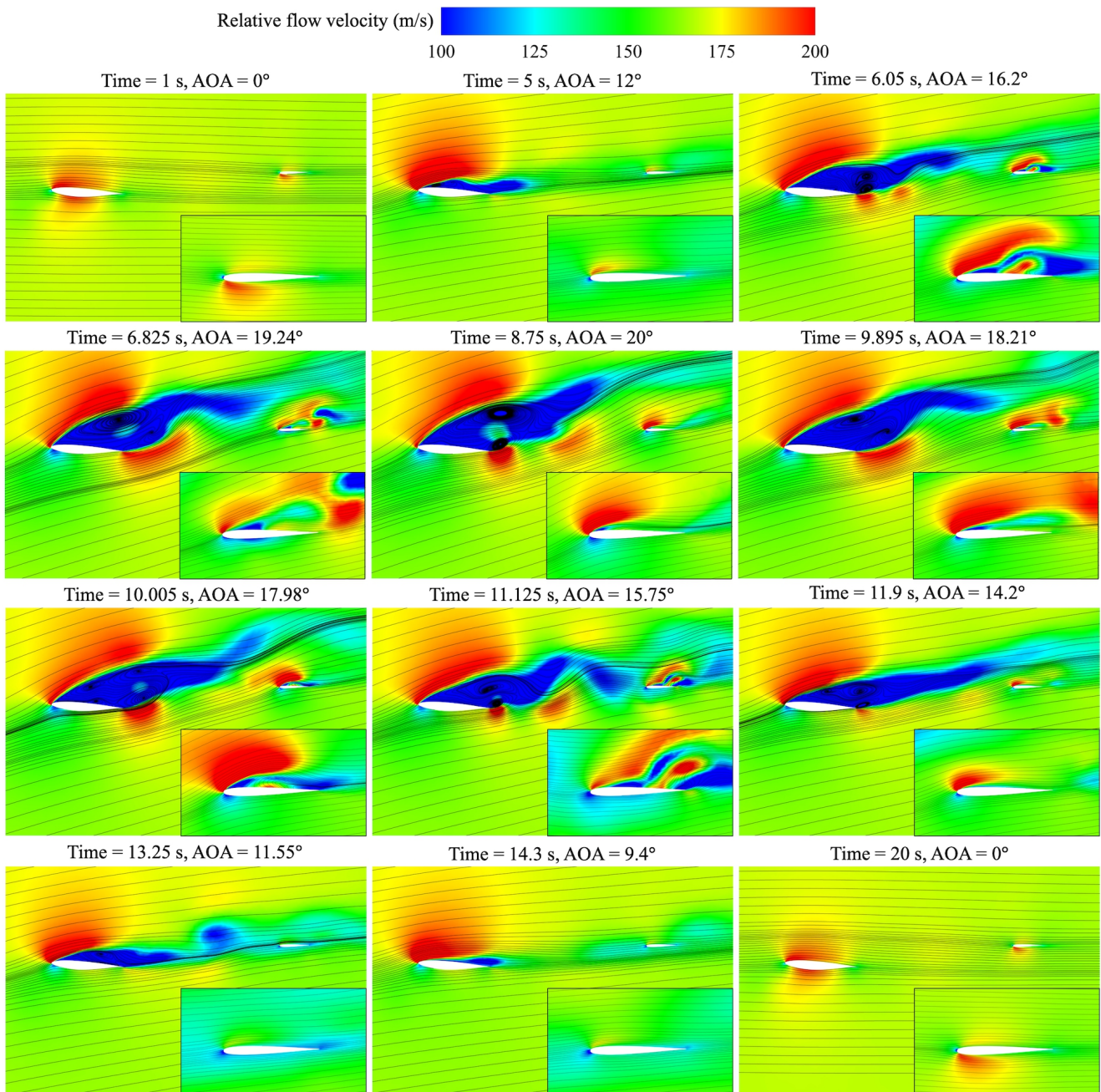
Fig. 7: Relative fluid velocity magnitude contour along the midspan of the horizontal tail showing the streamlines at different time instances. The view angle is rotated to align with the pitch angle.

while pitching up to 8° while pitching down is observed as aircraft tail buffeting [5].

The fluid velocity contour and streamlines along the midspan of the horizontal tail are shown in Figure 7, which provide insights into the formation of unsteady vortex cores as the flow separates behind the wing. The interaction between these vortices and the empennage of the aircraft results in the appearance of the observed buffeting phenomena. The turbulent wake violently impinges upon the hor-izontal tail during the pitch-down maneuver, as depicted in Figure 7, at angles of attack of 18.21° and 17.98°, which correspond to the maximum and minimum displacement of the tail, respectively. Additionally, Figure 8 shows the top view of the aircraft colored with pressure contour, demonstrating the non-uniform pressure distribution behind the wing and on the tail at different angles of attack. These findings are consistent with the effects of the separated flow behind the wing, as shown in Figure 7, that induce the observed buffeting phenomenon.
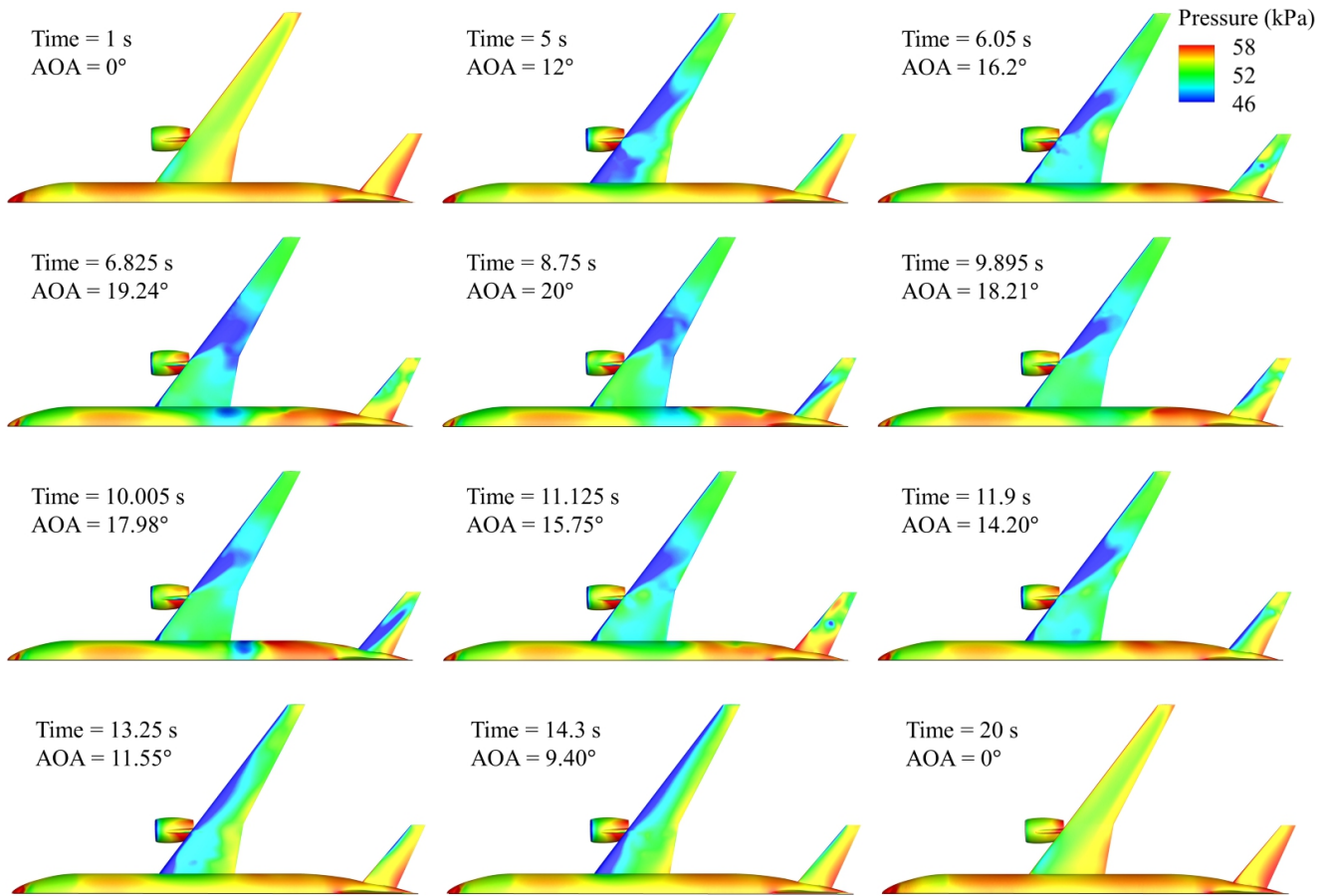
Fig. 8: Top view of the aircraft showing the pressure contour plot at different time instances.

4 Conclusions

This work presents a compressible flow FSI framework that is fully coupled and designed for nonmatching interface discretizations. The methodology's effectiveness for industrial-scale applications is demonstrated by simulating a full-scale aircraft's pitching movement to investigate tail buffeting phenomena. The simulation based on a prescribed angle of attack input has been successfully carried out using an ALE approach. The study presents both fluid and structural quantities of interest as a function of time and angle of attack. Based on the simulation results, it is evident that the unsteady dynamic flow behind the wing can cause nonlinear oscillations of the horizontal tail, especially at higher angles of attack. The tip displacement results indicate that at these angles, the tail experiences severe vibration, which is further amplified by dynamic fluid loads. Significant flow separation behind the wing can be seen from the airflow visualizations, which leads to flow disturbances observed in the tail region of the aircraft. The complex flow dynamics in the wake behind the wing result in the buffeting phenomenon, particularly at higher angles of attack, and understanding the dynamics of the wake is essential for developing effective methods to mitigate buffeting and enhance aircraft performance and safety. Further research is also necessary to investigate the effects of this phenomenon on structural fatigue and aircraft stability. Future work includes extending the framework to incorporate complex isogeometric fluid discretizations [67–72] to improve flow predictions especially in boundary layers, and to employ point cloud analysis methods to enable direct handling of as-manufactured or in-use objects and structures [73–75].

Acknowledgments

References

1. A. Abbas, J. Vicente, and E. Valero. Aerodynamic technologies to improve aircraft performance. *Aerospace Science and Technology*, 28:100–132, 2013.
2. A. Heinz, A. Haszler, C. Keidel, S. Moldenhauer, R. Benedictus, and W. S. Miller. Recent development in aluminium alloys for

aerospace applications. *Materials Science and Engineering: A*, 280:102–107, 2000.

3. J.-P. Immarigeon, R. T. Holt, A. K. Koul, L. Zhao, W. Wallace, and J. C. Beddoes. Lightweight materials for aircraft applications. *Materials Characterization*, 35:41–67, 1995.

4. B. H. K. Lee. Vertical tail buffeting of fighter aircraft. *Progress in Aerospace Sciences*, 36:193–279, 2000.

5. V. Sharma, J. Walker, M. Sweet, and T. Weimerskirch. P-3 aircraft buffet response characterization. In *39th AIAA Aerospace Science Meeting & Exhibition*, AIAA 2001-0711, Reno, Nevada, 2001.

6. N. F. Giannelis, G. A. Vio, and O. Levinski. A review of recent developments in the understanding of transonic shock buffet. *Progress in Aerospace Sciences*, 92:39–84, 2017.

7. L. Molent, R. Jones, S. Barter, and S. Pitt. Recent developments in fatigue crack growth assessment. *International Journal of Fatigue*, 28:1759–1768, 2006.

8. N. Liu, M. R. Rajanna, E. L. Johnson, J. Lua, N. Phan, and M.-C. Hsu. Isogeometric blended shells for dynamic analysis: simulating aircraft takeoff and the resulting fatigue damage on the horizontal stabilizer. *Computational Mechanics*, 70:1013–1024, 2022.

9. J. G. Marshall and M. Imregun. A review of aeroelasticity methods with emphasis on turbomachinery applications. *Journal of Fluids and Structures*, 10:237–267, 1996.

10. E. H. Dowell and K. C. Hall. Modeling of fluid–structure interaction. *Annual Review of Fluid Mechanics*, 33:445–490, 2001.

11. R. Kamakoti and W. Shyy. Fluid–structure interaction for aeroelastic applications. *Progress in Aerospace Sciences*, 40:535–558, 2004.

12. W. Shyy, H. Aono, S. K. Chimakurthi, P. Trizila, C.-K. Kang, C. E. S. Cesnik, and H. Liu. Recent progress in flapping wing aerodynamics and aeroelasticity. *Progress in Aerospace Sciences*, 46:284–327, 2010.

13. E. M. Lee-Rausch and J. T. Batina. Wing flutter boundary prediction using unsteady Euler aerodynamic method. *Journal of Aircraft*, 32(2), 1995.

14. C. Farhat and M. Lesoinne. Two efficient staggered algorithms for the serial and parallel solution of three-dimensional nonlinear transient aeroelastic problem. *Computer Methods in Applied Mechanics and Engineering*, 182:499–515, 2000.

15. M. J. Smith, D. H. Hodges, and C. E. S. Cesnik. Evaluation of computational algorithms suitable for fluid–structure interactions. *Journal of Aircraft*, 37(2), 2000.

16. J. N. Abras, C .E. Lynch, and M. J. Smith. Computational fluid dynamics–computational structural dynamics rotor coupling using an unstructured Reynolds-averaged Navier–Stokes methodology. *Journal of American Helicopter Society*, 57(1):1–14, 2012.

17. M. R. Rajanna, E. L. Johnson, N. Liu, A. Korobenko, Y. Bazilevs, and M.-C. Hsu. Fluid–structure interaction modeling with non-matching interface discretizations for compressible flow problems: computational framework and validation study. *Mathematical Models and Methods in Applied Sciences*, 32:2497–2528, 2022.

18. Y. Bazilevs, M.-C. Hsu, and M. A. Scott. Isogeometric fluid–structure interaction analysis with emphasis on non-matching discretizations, and with application to wind turbines. *Computer Methods in Applied Mechanics and Engineering*, 249–252:28–41, 2012.

19. F. Xu, G. Moutsanidis, D. Kamensky, M.-C. Hsu, M. Murugan, A. Ghoshal, and Y. Bazilevs. Compressible flows on moving domains: Stabilized methods, weakly enforced essential boundary conditions, sliding interfaces, and application to gas-turbine modeling. *Computers & Fluids*, 158:201–220, 2017.

20. M. R. Rajanna, E. L. Johnson, D. Codoni, A. Korobenko, Y. Bazilevs, N. Liu, J. Lua, N. Phan, and M.-C. Hsu. Finite element methodology for modeling aircraft aerodynamics: development, simulation, and validation. *Computational Mechanics*, 70: 549–563, 2022.

21. J. Kiendl, K.-U. Bletzinger, J. Linhard, and R. Wüchner. Isogeometric shell analysis with Kirchhoff–Love elements. *Computer Methods in Applied Mechanics and Engineering*, 198:3902–3914, 2009.

22. J. Kiendl, M.-C. Hsu, M. C. H. Wu, and A. Reali. Isogeometric Kirchhoff–Love shell formulations for general hyperelastic materials. *Computer Methods in Applied Mechanics and Engineering*, 291:280–303, 2015.

23. A. J. Herrema, E. L. Johnson, D. Proserpio, M. C. H. Wu, J. Kiendl, and M.-C. Hsu. Penalty coupling of non-matching isogeometric Kirchhoff–Love shell patches with application to composite wind turbine blades. *Computer Methods in Applied Mechanics and Engineering*, 346:810–840, 2019.

24. M.-C. Hsu and Y. Bazilevs. Fluid–structure interaction modeling of wind turbines: simulating the full machine. *Computational Mechanics*, 50:821–833, 2012.

25. M. C. H. Wu, D. Kamensky, C. Wang, A. J. Herrema, F. Xu, M. S. Pigazzini, A. Verma, A. L. Marsden, Y. Bazilevs, and M.-C. Hsu. Optimizing fluid–structure interaction systems with immersogeometric analysis and surrogate modeling: Application to a hydraulic arresting gear. *Computer Methods in Applied Mechanics and Engineering*, 316:668–693, 2017.

26. F. Xu, E. L. Johnson, C. Wang, A. Jafari, C.-H. Yang, M. S. Sacks, A. Krishnamurthy, and M.-C. Hsu. Computational investigation of left ventricular hemodynamics following bioprosthetic aortic and mitral valve replacement. *Mechanics Research Communications*, 112:103604, 2021.

27. G. E. Neighbor, H. Zhao, M. Saraeian, M.-C. Hsu, and D. Kamensky. Leveraging code generation for transparent immersogeometric fluid–structure interaction analysis on deforming domains. *Engineering with Computers*, 39:1019–1040, 2023.

28. J. Vassberg, M. Dehaan, M. Rivers, and R. Wahls. Development of a Common Research Model for applied CFD validation studies. In *AIAA 2008-6919*, Honolulu, Hawaii, 2008. 26th AIAA Applied Aerodynamics Conference.

29. M. B. Rivers and A. Dittberner. Experimental investigations of the NASA Common Research Model. *Journal of Aircraft*, 51:1183–1193, 2014.

30. NASA Common Research Model. https://commonresearchmodel. larc.nasa.gov/. [Accessed 31 March 2022].

31. F. Shakib, T. J. R. Hughes, and Z. Johan. A new finite element formulation for computational fluid dynamics: X. The compressible Euler and Navier–Stokes equations. *Comput. Methods Appl. Mech. and Engrg.*, 89:141–219, 1991.

32. G. J. Le Beau, S. E. Ray, S. K. Aliabadi, and T. E. Tezduyar. SUPG finite element computation of compressible flows with the entropy and conservation variables formulations. *Computer Methods in Applied Mechanics and Engineering*, 104:397–422, 1993.

33. S. K. Aliabadi and T. E. Tezduyar. Space–time finite element computation of compressible flows involving moving boundaries and interfaces. *Computer Methods in Applied Mechanics and Engineering*, 107:209–223, 1993.

34. T. E. Tezduyar, S. K. Aliabadi, M. Behr, and S. Mittal. Massively parallel finite element simulation of compressible and incompressible flows. *Computer Methods in Applied Mechanics and Engineering*, 119:157–177, 1994.

35. G. Hauke and T. J. R. Hughes. A unified approach to compressible and incompressible flows. *Computer Methods in Applied Mechanics and Engineering*, 113:389–396, 1994.

36. G. P. Wren, S. E. Ray, S. K. Aliabadi, and T. E. Tezduyar. Space–time finite element computation of compressible flows between moving components. *International Journal for Numerical Methods in Fluids*, 21:981–991, 1995.

37. G. P. Wren, S. E. Ray, S. K. Aliabadi, and T. E. Tezduyar. Simulation of flow problems with moving mechanical components, fluid–structure interactions and two-fluid interfaces. *International*

Journal for Numerical Methods in Fluids, 24:1433–1448, 1997.

38. S. Mittal and T. Tezduyar. A unified finite element formulation for compressible and incompressible flows using augumented conservation variables. *Computer Methods in Applied Mechanics and Engineering*, 161:229–243, 1998.

39. S. E. Ray and T. E. Tezduyar. Fluid–object interactions in interior ballistics. *Computer Methods in Applied Mechanics and Engineering*, 190:363–372, 2000.

40. G. Hauke. Simple stabilizing matrices for the computation of compressible flows in primitive variables. *Computer Methods in Applied Mechanics and Engineering*, 190:6881–6893, 2001.

41. T. J. R. Hughes, G. Scovazzi, and T. E. Tezduyar. Stabilized methods for compressible flows. *Journal of Scientific Computing*, 43:343–368, 2010.

42. K. Takizawa, T. E. Tezduyar, and T. Kanai. Porosity models and computational methods for compressible-flow aerodynamics of parachutes with geometric porosity. *Mathematical Models and Methods in Applied Sciences*, 27:771–806, 2017.

43. T. Kanai, K. Takizawa, T. E. Tezduyar, T. Tanaka, and A. Hartmann. Compressible-flow geometric-porosity modeling and spacecraft parachute computation with isogeometric discretization. *Computational Mechanics*, 63:301–321, 2019.

44. K. Takizawa, Y. Otoguro, and T. E. Tezduyar. Variational multiscale method stabilization parameter calculated from the strain-rate tensor. *Mathematical Models and Methods in Applied Sciences*, 33:1661–1691, 2023.

45. T. E. Tezduyar and Y. J. Park. Discontinuity capturing finite element formulations for nonlinear convection–diffusion–reaction equations. *Computer Methods in Applied Mechanics and Engineering*, 59:307–325, 1986.

46. T. J. R. Hughes, M. Mallet, and A. Mizukami. A new finite element formulation for computational fluid dynamics: II. Beyond SUPG. *Computer Methods in Applied Mechanics and Engineering*, 54:341–355, 1986.

47. T. J. R. Hughes and M. Mallet. A new finite element formulation for computational fluid dynamics: IV. A discontinuity-capturing operator for multidimensional advective–diffusive systems. *Computer Methods in Applied Mechanics and Engineering*, 58:329–339, 1986.

48. R. C. Almeida and A. C. Galeão. An adaptive Petrov–Galerkin formulation for the compressible Euler and Navier–Stokes equations. *Computer Methods in Applied Mechanics and Engineering*, 129:157–176, 1996.

49. G. Hauke and T. J. R. Hughes. A comparative study of different sets of variables for solving compressible and incompressible flows. *Computer Methods in Applied Mechanics and Engineering*, 153:1–44, 1998.

50. T. E. Tezduyar and M. Senga. Stabilization and shock-capturing parameters in SUPG formulation of compressible flows. *Computer Methods in Applied Mechanics and Engineering*, 195:1621–1632, 2006.

51. T. E. Tezduyar, M. Senga, and D. Vicker. Computation of inviscid supersonic flows around cylinders and spheres with the SUPG formulation and YZβ shock-capturing. *Computational Mechanics*, 38:469–481, 2006.

52. T. E. Tezduyar and M. Senga. SUPG finite element computation of inviscid supersonic flows with YZβ shock-capturing. *Computers & Fluids*, 36:147–159, 2007.

53. F. Rispoli, R. Saavedra, A. Corsini, and T. E. Tezduyar. Computation of inviscid compressible flows with the V-SGS stabilization and YZβ shock-capturing. *International Journal for Numerical Methods in Fluids*, 54:695–706, 2007.

54. F. Rispoli, R. Saavedra, F. Menichini, and T. E. Tezduyar. Computation of inviscid supersonic flows around cylinders and spheres with the V-SGS stabilization and YZβ shock-capturing. *Journal of Applied Mechanics*, 76:021209, 2009.

55. F. Rispoli, G. Delibra, P. Venturini, A. Corsini, R. Saavedra, and T. E. Tezduyar. Particle tracking and particle–shock interaction in compressible-flow computations with the V-SGS stabilization and YZβ shock-capturing. *Computational Mechanics*, 55:1201–1209, 2015.

56. K. Takizawa, T. E. Tezduyar, and Y. Otoguro. Stabilization and discontinuity-capturing parameters for space–time flow computations with finite element and isogeometric discretizations. *Computational Mechanics*, 62:1169–1186, 2018.

57. J. Chung and G. M. Hulbert. A time integration algorithm for structural dynamics with improved numerical dissipation: The generalized-α method. *Journal of Applied Mechanics*, 60:371–75, 1993.

58. K. E. Jansen, C. H. Whiting, and G. M. Hulbert. A generalized-α method for integrating the filtered Navier-Stokes equations with a stabilized finite element method. *Computer Methods in Applied Mechanics and Engineering*, 190:305–319, 2000.

59. Y. Bazilevs, V. M. Calo, T. J. R. Hughes, and Y. Zhang. Isogeometric fluid–structure interaction: theory, algorithms, and computations. *Computational Mechanics*, 43:3–37, 2008.

60. T. E. Tezduyar, S. Sathe, R. Keedy, and K. Stein. Space–time finite element techniques for computation of fluid–structure interactions. *Computer Methods in Applied Mechanics and Engineering*, 195:2002–2027, 2006.

61. T. E. Tezduyar, S. Sathe, and K. Stein. Solution techniques for the fully-discretized equations in computation of fluid–structure interactions with the space–time formulations. *Computer Methods in Applied Mechanics and Engineering*, 195:5743–5753, 2006.

62. T. E. Tezduyar and S. Sathe. Modelling of fluid–structure interactions with the space–time finite elements: Solution techniques. *International Journal for Numerical Methods in Fluids*, 54(6–8):855–900, 2007.

63. A. A. Johnson and T. E. Tezduyar. Mesh update strategies in parallel finite element computations of flow problems with moving boundaries and interfaces. *Computer Methods in Applied Mechanics and Engineering*, 119:73–94, 1994.

64. K. Stein, T. Tezduyar, and R. Benney. Mesh moving techniques for fluid–structure interactions with large displacements. *Journal of Applied Mechanics*, 70:58–63, 2003.

65. K. Stein, T. E. Tezduyar, and R. Benney. Automatic mesh update with the solid-extension mesh moving technique. *Computer Methods in Applied Mechanics and Engineering*, 193:2019–2032, 2004.

66. Y. Bazilevs, M.-C. Hsu, J. Kiendl, R. Wüchner, and K.-U. Bletzinger. 3D simulation of wind turbine rotors at full scale. Part II: Fluid–structure interaction modeling with composite blades. *International Journal for Numerical Methods in Fluids*, 65:236–253, 2011.

67. K. Takizawa, T. E. Tezduyar, H. Uchikawa, T. Terahara, T. Sasaki, and A. Yoshida. Mesh refinement influence and cardiac-cycle flow periodicity in aorta flow analysis with isogeometric discretization. *Computers & Fluids*, 179:790–798, 2019.

68. T. Terahara, K. Takizawa, T. E. Tezduyar, A. Tsushima, and K. Shiozaki. Ventricle-valve-aorta flow analysis with the Space–Time Isogeometric Discretization and Topology Change. *Computational Mechanics*, 65:1343–1363, 2020.

69. Y. Bazilevs, K. Takizawa, M. C. H. Wu, T. Kuraishi, R. Avsar, Z. Xu, and T. E. Tezduyar. Gas turbine computational flow and structure analysis with isogeometric discretization and a complex-geometry mesh generation method. *Computational Mechanics*, 67:57–84, 2021.

70. L. Aydinbakar, K. Takizawa, T. E. Tezduyar, and D. Matsuda. U-duct turbulent-flow computation with the ST-VMS method and isogeometric discretization. *Computational Mechanics*, 67:823–843, 2021.

71. T. Kuraishi, Z. Xu, K. Takizawa, T. E. Tezduyar, and S. Yamasaki. High-resolution multi-domain space–time isogeometric analysis

of car and tire aerodynamics with road contact and tire deformation and rotation. *Computational Mechanics*, 70:1257–1279, 2022.

72. Y. Bazilevs, K. Takizawa, T. E. Tezduyar, A. Korobenko, T. Kuraishi, and Y. Otoguro. Computational aerodynamics with isogeometric analysis. *Journal of Mechanics*, 39:24–39, 2023.

73. L. Kudela, S. Kollmannsberger, U. Almac, and E. Rank. Direct structural analysis of domains defined by point clouds. *Computer Methods in Applied Mechanics and Engineering*, 358:112581, 2020.

74. A. Balu, M. R. Rajanna, J. Khristy, F. Xu, A. Krishnamurthy, and M.-C. Hsu. Direct immersogeometric fluid flow and heat transfer analysis of objects represented by point clouds. *Computer Methods in Applied Mechanics and Engineering*, 404:115742, 2023.

75. X. Wang, M. Jaiswal, A. M. Corpuz, S. Paudel, A. Balu, A. Krishnamurthy, J. Yan, and M.-C. Hsu. Photogrammetry-based computational fluid dynamics. *Computer Methods in Applied Mechanics and Engineering*, 417:116311, 2023.